Development of a flexure-based nano-actuator for high-frequency high-resolution directional sensing with atomic force microscopy

Amir F. Payam, Luca Piantanida and Kislon Voïtchovsky

View Online   Export Citation   CrossMark

ARTICLES YOU MAY BE INTERESTED IN

Development of a flexure-based nano-actuator for high-frequency high-resolution directional sensing with atomic force microscopy

View Online   Export Citation   CrossMark

Amir F. Payam,[a)] (iD) **Luca Piantanida,**[b)] (iD) and **Kislon Voïtchovsky**[c)] (iD)

AFFILIATIONS

Department of Physics, Durham University, Durham DH1 3LE, United Kingdom

[a)]**Present address:** Nanotechnology and Integrated Bioengineering Centre (NIBEC), School of Engineering,
Ulster University, Jordanstown Shore Road, Northern Ireland BT37 0QB, United Kingdom.
[b)]**Present address:** Micron School of Materials Science and Engineering, Boise State University, 1910 W University Dr, Boise,
Idaho 83725, USA.
[c)]**Author to whom correspondence should be addressed:** kislon.voitchovsky@durham.ac.uk

ABSTRACT

Scanning probe microscopies typically rely on the high-precision positioning of a nanoscale probe in order to gain local information about the properties of a sample. At a given location, the probe is used to interrogate a minute region of the sample, often relying on dynamical sensing for improved accuracy. This is the case for most force-based measurements in atomic force microscopy (AFM) where sensing occurs with a tip oscillating vertically, typically in the kHz to MHz frequency regime. While this approach is ideal for many applications, restricting dynamical sensing to only one direction (vertical) can become a serious limitation when aiming to quantify the properties of inherently three-dimensional systems, such as a liquid near a wall. Here, we present the design, fabrication, and calibration of a miniature high-speed scanner able to apply controlled fast and directional in-plane vibrations with sub-nanometer precision. The scanner has a resonance frequency of ~35 kHz and is used in conjunction with a traditional AFM to augment the measurement capabilities. We illustrate its capabilities at a solid–liquid interface where we use it to quantify the preferred lateral flow direction of the liquid around every sample location. The AFM can simultaneously acquire high-resolution images of the interface, which can be superimposed with the directional measurements. Examples of sub-nanometer measurements conducted with the new scanner are also presented.

I. INTRODUCTION

Nano-positioning systems have a wide range of applications in micro- and nano-technologies, from MEMS[1] to the nano-manipulation of samples[2] and lithographic applications.[3] Part of the drive for the development of nano-actuators and a positioning system comes from the advent of scanning probe microscopies[4–6] (SPMs) where a nanoscale probe is used to quantify various properties of a given sample locally as it travels across the sample's surface.[7–9] In most systems, the lateral positioning of the probe is carried out using piezo actuators mounted in a dedicated scanner. The scanner is able to move the probe in all directions with respect to the sample, with modern systems achieving routinely sub-angstrom positioning precision.[10–13] Scanning probe microscopies often conduct measurements dynamically to improve accuracy or

access information otherwise not available, such as time-dependent quantities. A typical example is the vibrating tip often used in atomic force microscopy (AFM) to probe the topography and the mechanical properties of a given sample, often with atomic- or molecular-level resolution.[7,14–17] The AFM has emerged as a tool of choice for visualizing, characterizing, and manipulating samples at the nanoscale,[18–21] also in the liquid environment thanks to its ability to function with non-conducting samples.[17,22–30] In AFM measurements, the nano-sharp tip is mounted on a flexible cantilever whose deflection is used to quantify the force experienced by the tip. Dynamical measurements are typically achieved by actively vibrating the cantilever, often at one of its eigenmodes for increased sensitivity to tip–sample interactions.[19,31–33] Any change in the vibration amplitude, frequency, and phase is quantified with a lock-in amplifier. Due to the use of a cantilever, the tip oscillation is mainly

limited to a vertical or torsional motion. In all cases, the dynamic sensing is inherently unidirectional, determined by the geometry of the cantilever's vibration.

While sufficient for many applications, this unidirectional sensing can become a serious limitation when investigating intrinsically three-dimensional systems: samples where the relevant properties in each direction are independent from each other or only lightly coupled. This is often the characteristic of soft materials or liquid samples. For example, when considering a liquid near a wall, a vertically vibrating tip can only probe changes in the liquid's nanoscale viscoelastic behavior perpendicular to the wall.[22,34–36] This is arguably the less relevant information with no possibility to quantify the properties of the flow parallel to the wall.[37–42] Even in solid systems, it is sometimes useful to probe interactions that are not necessarily perpendicular to the surface but rather along a set arbitrary direction.[43]

Currently, multidirectional probing is highly challenging due to the inherently unidirectional geometry of standard AFM cantilevers. Overcoming this limitation can be achieved by adding a lateral component to the otherwise purely vertical vibration of the tip, with the lateral oscillation being set in any desired direction within the horizontal plane (i.e., perpendicular to the vertical tip oscillation). In this manner, the composed motion of the vibrating tip is effectively three-dimensional, along a set direction. This could, in principle, be achieved with a standard XY scanner by imposing a small directional oscillation at the desired frequency around the set tip position. However, to be meaningful, the oscillation would have to be comparable in frequency and amplitude to the vertical tip oscillation, which typically ranges from tens to hundreds of kilohertz. Operating a scanner at such high frequencies is far from trivial due to the scanner inertia, intrinsic resonances, and the heat dissipation of the piezo elements. A typical modern SPM scanner exhibits resonances between 2 and 10 kHz. There are hence considerable research efforts to improve the speed of operation, measurement precision, and bandwidth.[44–50] With video-rate AFMs, measurements are now possible, also in solution.[51–58] To date, existing solutions are still too slow for the frequencies of interest here (>20 kHz), partly because the emphasis is placed on accurate positioning over several micrometers instead of the small (<10 nm) amplitudes needed here.

In order to tackle this challenge, we develop a fast 2D flexure-based actuator stage capable of operating at frequencies of up to 40 kHz over amplitudes <5 nm and able to carry a typical AFM sample (Fig. 1).

This high-frequency actuator stage (hereafter referred to as the high-frequency stage, HF-stage, for clarity) is designed small enough to fit directly on top of a standard AFM scanner so as to add a fast, directional oscillation to the normal raster motion of the standard scanner (Fig. 1). The emphasis is placed on high-frequency operation and compactness to fit easily onto commercial AFM scanners in order to augment their capabilities. To optimize the design of the HF-stage and identify the optimum material and geometrical parameters, we extensively used finite elements analysis (FEA) with the ANSYS software (Ansys Inc., Pittsburgh, USA). The physical stage was built based on the simulations and calibrated, and its performance was assessed against the theoretical predictions. Since the HF-stage is intended for working in conjunction with the AFM, we also investigate the stage's impact on imaging resolution and noise under typical operation conditions. Finally, we briefly illustrate
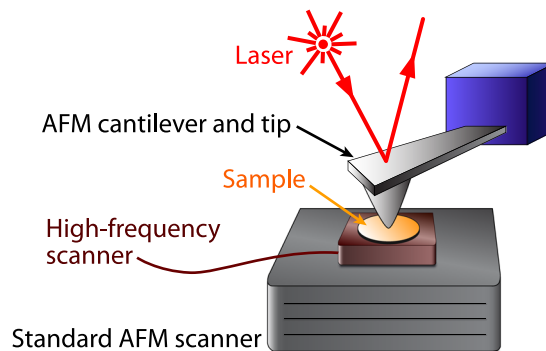
FIG. 1. Schematic representation of the high-frequency actuator stage developed in this paper for directional dynamical sensing. The stage is intended for operation in conjunction with a standard AFM three-dimensional scanner with the motions of the stage and the scanner being additive.

the measurement capabilities of the HF-stage by using it to derive the directional flow map of aqueous solutions at the interface with graphene oxide (GO).

The emphasis of this paper is placed on the development and characterization of this HF-stage. Integrating the stage into AFM measurements so as to derive meaningful information can require further developments in terms of synchronization with the AFM and data analysis, which is presented elsewhere in detail.[59]

II. RESULTS

A. Design and development of the high-frequency flexure-based XY stage

In order to develop an actuating stage able to function reliably at high frequencies, it is necessary to take into account several limiting factors, such as (i) the dynamic behavior of the actuator, (ii) the bandwidth of the driving amplifier, (iii) the bandwidth of the feedback control system, and (iv) the speed of the data acquisition system.[48,51,60] Several studies have improved the AFM technology to compensate for these limitations[45,47,49,60–70] but not at such high frequencies of interest here. Examples include the introduction of fast actuators with advanced feed-forward control techniques.[48,66,68,70,71] The design and assembly of the actuators are also important points to consider, for example, using mechanically stiffness and compact stages helps minimize the need for advanced motion correction,[47,48,60,69] in particular for high speed nanopositioning.[13,63–65,72,73] Piezoelectric-based actuators are commonly used in scanning probe microscopes[11,46,51,70] owing to their high speed, compact size, high intrinsic stiffness, lack of internal friction on displacement, and high positioning resolution. Scanners are typically constructed from piezoelectric tube actuators,[10,11] shear piezo actuators, or piezoelectric stack actuators.[49] Tube scanners, although frequently used in conventional AFM scanners, have a low resonance frequency and are hence not suitable for high-speed actuation. In contrast, shear piezo actuators offer a compact design with a high mechanical resonance and bandwidth operation, although at the cost of the displacement range.[51] The latter can be improved using a stacked design that results in a better voltage-to-displacement ratio but at the cost of a coupling between the latter and vertical motion.

Once suitable piezos are selected, they are assembled into the scanner. Different designs for high-speed scanners have been proposed,[49,74–76] for instance, counterbalanced scanners,[65] micro-resonator scan stages,[68] and flexure-based scanners.[49,75,76] Flexure-based scanners offer the advantage of high mechanical resonances and low cross-coupling.[77] The absence of moving and sliding joints in flexure-based stage design can eliminate the problems related to wear, backlash, and friction.[11,77–79] Moreover, the flexure-guided mechanism also offers the advantage of using monolithic materials without any assembly of links and joints.[77] Here, the main objectives of our design are as follows:

- High resonance frequency for a small displacement (typically <10 nm) so as to produce modulated sinusoidal motion of comparable amplitude in both the X and Y directions.
- Compact design with dimensions of less than 16 mm length and width and 3 mm height to fit in most existing commercial AFMs.
- The HF-stage should be rigid and as light as possible to accommodate various types of samples while limiting the impact of inertia due to the added mass.

Flexures in the nanopositioning stage provide motion in the desired directions through the elastic deformation of the stage.[51,78] Here, four piezoelectric stack actuators are used to drive the motion of the flexure-based HF-stage's X and Y axes. While it is not necessary to use four actuators, they provides us with a simple mean to drive and probe the stage simultaneously. We use beam-like flexures to guide the stage along the direction of the actuator motion. The piezo elements are usually glued on or clamped tightly on a stage. Here, we glued them to the stage using two component epoxy resin (Araldite Standard, Huntsman Advanced Materials, Basel, Switzerland). It is necessary for the HF-stage to be electrically insulated for operation in liquids and to have thermal sinks to dissipate the heat generated during normal operation. The resin was therefore also used to cover and insulate the electrical contacts. A schematic representation of the retained HF-stage design is given in Fig. 2, from the ANSYS analysis.

To find a suitable compromise between the resonance frequency and travel range, we used the finite element method. The numerical simulation, design optimization, and characterization of the HF-stage dynamic behavior were carried out using ANSYS with several design iterations to reach the stated objectives. The optimum values for thickness, width, and length of flexures are 2.5, 0.5, and 2 mm, respectively. Figure 2(b) shows the graphical representation of the X and Y motions of the stage simulated with ANSYS (131 537 nodes and 84 667 elements). Since the resonance frequency of the HF-stage is dependent on the type of the material used, we investigated several common materials for the stage body.[65] The ANSYS predictions for the X and Y resonance frequencies, stiffness, and weight of the stage for each material are given in Table I.

The total resonance frequency of the combined flexure-based stage with a piezoelectric actuator can be modeled as a mass–spring system, in series with the stage in each direction. The natural resonance frequency of the combined system can be approximated as[78,79]

$$f = \frac{1}{2\pi}\sqrt{\frac{k_s + k_p}{M_s + M_p/2}}, \tag{1}$$
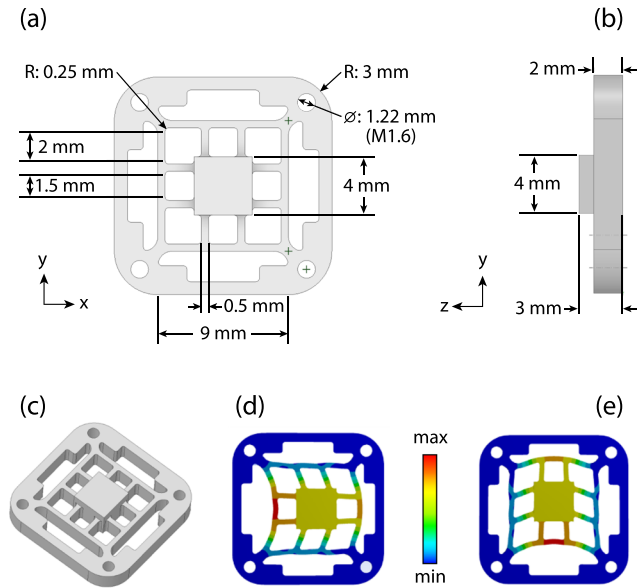
FIG. 2. Detailed structure of the HF-stage with top (a) and side (b) views. The sizes of the different features are given in metric units. (c) 3D-rendering of the stage design. (d) and (e) Finite element simulation and stiffness estimation of the XY scanner for aluminum alloy along the x and y directions, respectively. The color scale represents the degree of deformation across the HF-stage during operation as calculated using ANSYS (arbitrary units).

where k_s is the effective stiffness of all flexures, k_p is the stiffness of the piezo actuator, M_s is the mass of the stage, and $M_p/2$ approximates the mass contribution of the moving piezoelectric actuator. The travel range of the stage is obtained as[78]

$$\Delta L = \frac{k_p}{k_s + k_p}L_0, \tag{2}$$

where L_0 is the unloaded travel range of the piezoelectric actuator. The X and Y resonance frequencies of the combined flexure-based stage and piezoelectric actuator based on the stiffness and mass of the piezo actuator are shown in Fig. 3. For a lighter and stiffer piezo actuator, the total frequency can increase to ~90 kHz for structural steel, stainless steel, and copper alloy materials and ~150 kHz for aluminum alloy. Generally, choosing a light and stiff piezo actuator leads to the increase in the total frequency of the combined stage with the piezo actuator, as expected.

TABLE I. ANSYS predictions for the HF-stage X and Y resonance frequency $f_{x,y}$, mass, and stiffness $k_{x,y}$ considering different body materials.

Material	$f_{x,y}$ (kHz)	Mass (g)	$k_{x,y}$ (N/μm)
Structural steel	34.3	1.96	22.1
Stainless steel	33.9	1.93	21.4
Aluminum alloy	34.7	0.69	7.9
Copper alloy	25.0	2.07	12.3
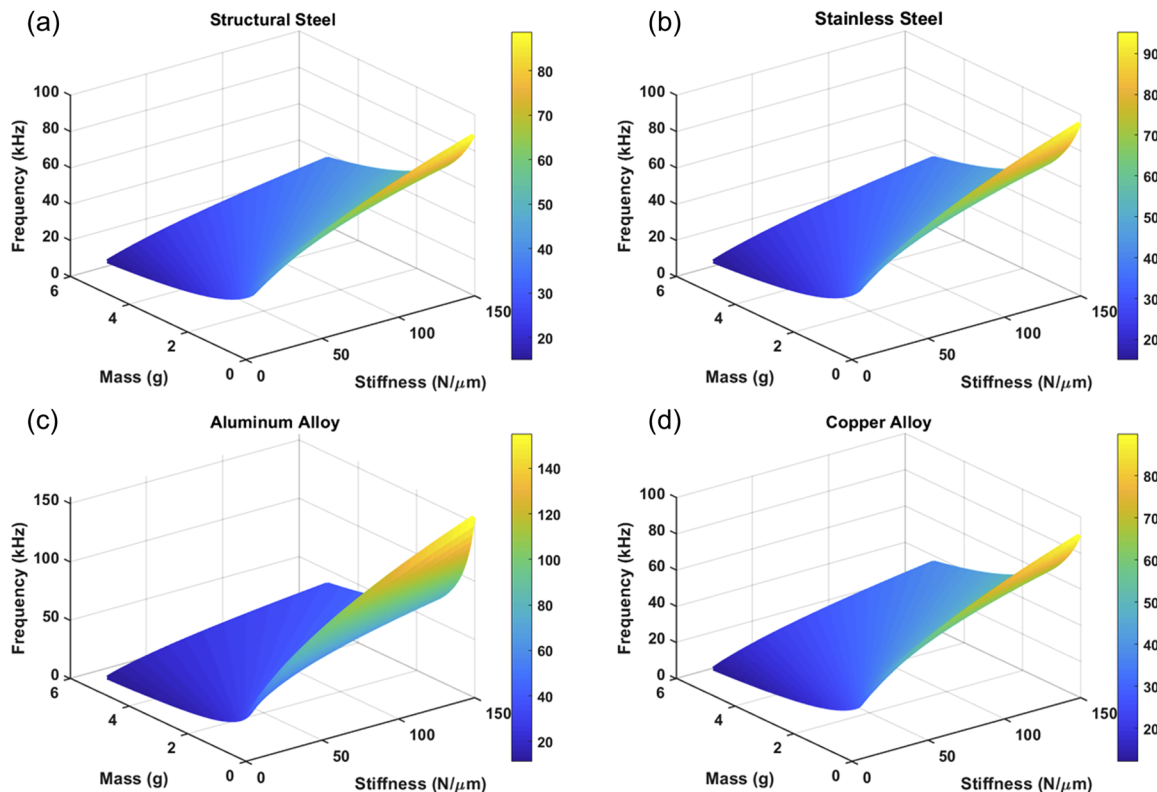
FIG. 3. Mechanical resonance frequencies of the combined stage with the piezo actuator in relation to the mass and stiffness of the piezo actuator for different materials simulated with ANSYS. The results are shown for (a) structural steel, (b) stainless steel, (c) aluminum alloy, and (d) copper alloy.

The proportional ratios of stage motion to the piezo travel range are shown in Fig. 4 for the different materials as a function of mass and stiffness of the piezo actuator. From Fig. 4, it is immediately clear that the stiffer piezo offers a longer travel range. In addition, the travel range for the aluminum alloy stage is larger than that for the other materials.

Based on these results, we selected the aluminum alloy to construct the HF-stage. We also note that to achieve a resonance frequency of ~100 kHz, we need piezo actuators with a stiffness >50 N/μm and as light as possible.

B. Fabrication, testing, and characterization of the nanopositioner

Using the design results predicted using ANSYS, the HF-stage was fabricated using Al 7075 alloy with a thickness of 2.5 mm by standard Computer Numerical Control (CNC) milling. Figure 5 shows the final product, including a sample mounted on a thin 10 mm diameter steel disk. Given the relatively high operation frequencies of the stage, it is crucial for the sample to be attached tightly and stiffly to the stage so as to follow its movements. Here, this was achieved by gluing the sample onto the scanner using a relatively low surface tension epoxy (Epo-Tek 353ND, Billerica, MA, USA) that allows a binding layer to be as thin as possible. The mass of the samples used was always well below 1 g,

including the steel disk. A British one-pound (£1) coin is shown to illustrate the size of the miniature scanner. The actuation of the stage is ensured by four piezoelectric stack actuators (miniature multilayer piezo actuators, PL022.3x PICMA, Physik Instrumente, Karlsruhe, Germany). The blocking force of the piezos is rated at 120 N, the maximum travel range is 2.2 μm, the operating voltage range is between −20 and 100 V, and the axial resonance frequency of piezos is above 600 kHz. The piezo actuators are glued in place with epoxy resin (Araldite Standard, Basel, Switzerland) and driven directly through a Data Acquisition Board with BNC terminations (NI USB-6366, X Series DAQ Device, National Instruments, Austin, TX, USA) by a program created using the software Labview (National Instruments, Austin, TX, USA). Since the HF-stage is designed for small amplitude lateral oscillations, the voltages applied to the piezo actuators rarely exceed 1–2 V, bypassing the need for an amplifier. To test the performance of the HF-stage, we need to experimentally verify its natural frequency and its displacement and assess the accuracy of its nano-positioning at different frequencies and amplitudes for a set desired motion. To characterize the frequency response of the HF-stage to a given drive signal, the desired signal is applied to two of the piezoelectric stack actuators along the X and Y directions, with the counter piezo elements used as sensors to measure the resulting displacement and its relative amplitude.
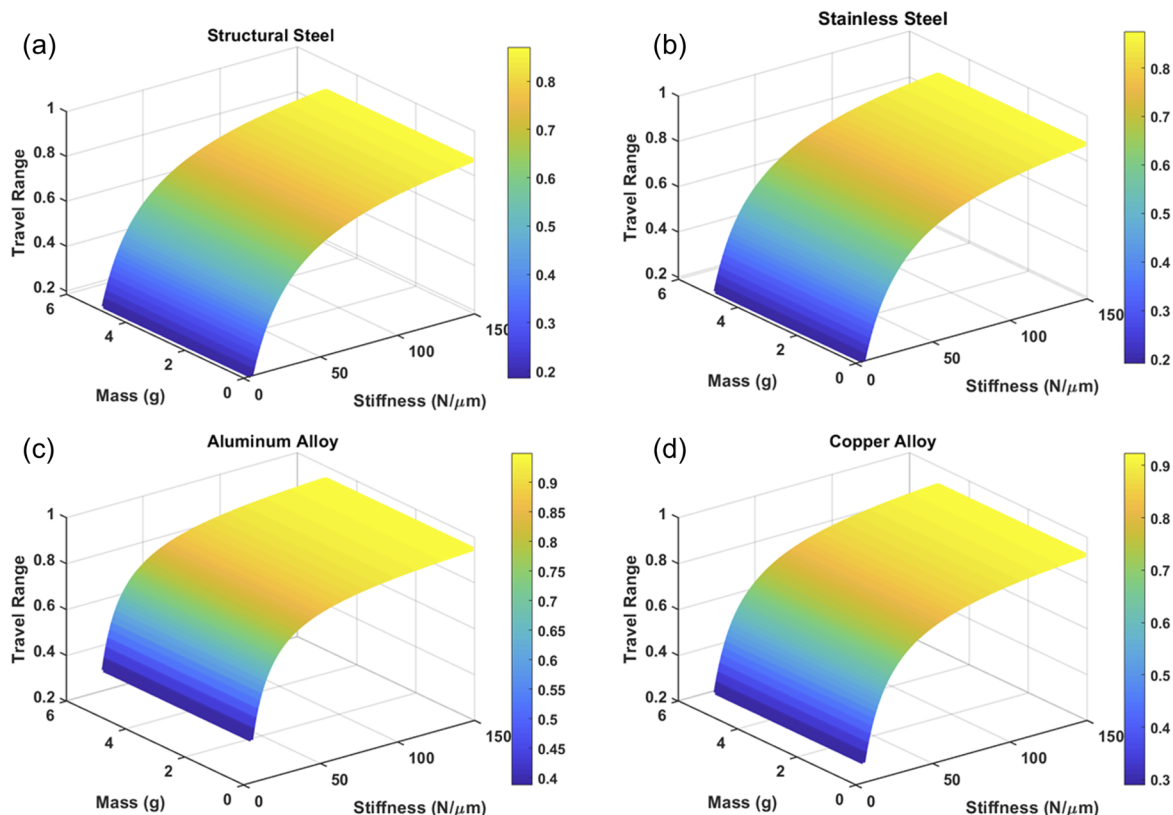
FIG. 4. Proportional travel range ratio of the combined stage with the piezo actuator in relation to the mass and stiffness of the piezo actuator for different body materials, as simulated with ANYSIS. The results are presented for (a) structural steel, (b) stainless steel, (c) aluminum alloy, and (d) copper alloy.
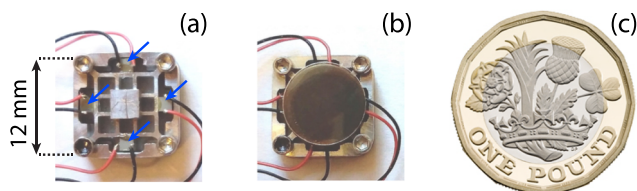
1. Resonance frequency characterization

To characterize the frequency response of the HF-stage, a random noise was applied to one of the piezo-stack actuators as input [Fig. 6(a)], and its effect was measured on its counter-piezo [Fig. 6(b)]. The random noise signal (4 V amplitude) was generated using Labview and fed through a data acquisition system (DAQ). The first resonant peak of the stage is observed at around 35 kHz at both axes, in agreement with ANSYS simulation results. A better characterization of the HF-stage's resonance and cross-coupling between its perpendicular axes can be performed by driving a piezo stack actuator with a low frequency sinusoidal signal (1 Hz and

4 V amplitude) and measuring the spectral output of the counter [Fig. 6(c)] and cross [Fig. 6(d)] piezo. As visible from Fig. 6(c), the first resonance frequency of the HF-stage lies around 35 kHz and the magnitude of the cross-coupling term is about −35 dB less than that of direct coupling [Fig. 6(d)]. Overall, the discrepancy between finite element analysis predictions and the measured resonance is less than 5%.

2. Dynamic response characterization

Since the purpose of the HF-stage is to operate at high frequencies, we evaluated the stage's performance in tracking a simple sinusoidal signal with a frequency of 1 kHz and an amplitude of 1 V (Fig. 7). It is immediate from Fig. 7 that the stage follows the input without a problem or added noise, except at the resonance (Fig. 7, dashed line).

In reality, the planned dynamic operation of the HF-stage is more complex, with modulated oscillations in the X and Y directions to probe every in-plane direction around a given location. In a standard dynamical AFM measurement, the probe oscillates vertically around a given location and with small oscillations (<1 nm) in order to achieve satisfactory spatial accuracy. Here, the same principle holds with the HF-stage used to impose a small directional lateral (in-plane) oscillation around the probe's location. The location itself is set by positioning with the standard AFM scanner (Fig. 1). The

FIG. 5. Picture of the finished flexural scanner with the four piezo elements highlighted with blue arrows (a) and a typical AFM sample mounted on the scanner (b). For comparison, a £1 British coin (c) is shown to scale.
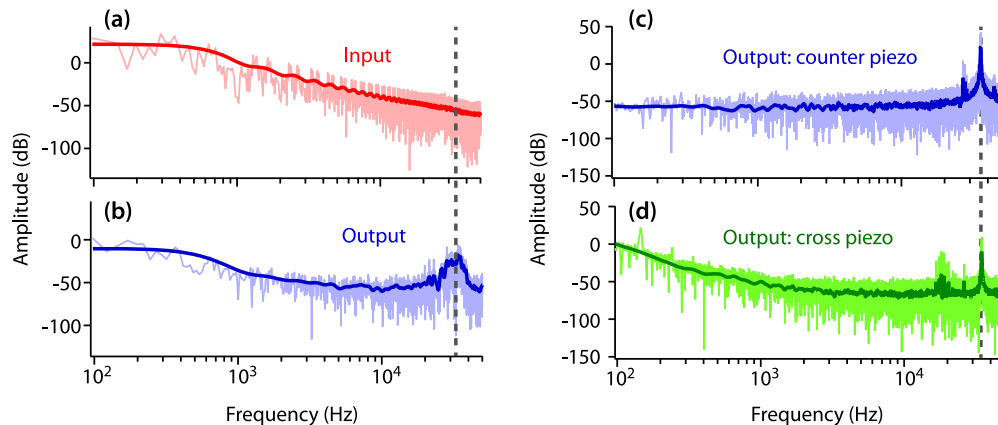
FIG. 6. Frequency characterization of the HF-stage. When a random noise is applied to one of the piezo actuators (a), its counter piezo reveals the hint of a resonance around 35 kHz (b). The same experiment carried out with a sinusoidal 1 Hz, 4 V input evidences the resonance in direct [counter piezo (c)] and cross [cross piezo (d)] configurations, with a cross-coupling about −35 dB lower than the direct axis.

frequency, amplitude, and direction of the HF-stage's oscillation are determined by the sinusoidal signals imposed to the X and Y piezo stacks with the motions in both directions adding up geometrically. The same high frequency is used for both directions, and the total amplitude of the oscillation is simply the geometrical average of the amplitudes A_X and A_Y. To probe a set direction, the phase between the X and Y oscillations must be set to zero (or π). In practice, it is useful to probe all the possible lateral directions at a given location. This can be achieved using modulated X and Y oscillations. The faster oscillation (frequency ν_{sweep}) imposes a rapid lateral sweep of the tip along a given direction. The slower oscillation (frequency ν_{vortex}) progressively changes the direction of the sweep, systematically exploring all the possible in-plane directions over its period (see Ref. 59 for more details). The lateral velocity of the tip with respect to the sample needs to be comparable to that of the vertical tip motion to derive meaningful data. This approach, called "vortex" scanning,

was successfully used recently to probe the flow patterns of liquids at interfaces.[59] With this in mind, a modulated sinusoidal signal was applied to the piezo actuators while tracking the motion of the stage with the counter piezo. Here, the high frequency "sweep" signal is sinusoidal at 20 kHz with the "vortex" modulation sinusoidal set at 1 kHz and 1 V amplitude [Fig. 8(a)]. Due to the modulated frequency, two spectral peaks are visible at 19 and 21 kHz, demonstrating that the HF-stage can provide the desired motion. This is confirmed in the time domain with the stage following faithfully the input modulated oscillation [Fig. 8(b)].

### C. Calibration of the HF-stage

The calibration of the HF-stage is a fundamental step to determine the true amplitude of the oscillation along X and Y axes. This information is key to control the direction of any displacement and its amplitude. Given the intrinsic variability in the voltage-induced displacement of the piezo crystals, a calibration has to be carried every time the nanopositioner is updated or a crystal is replaced. Two calibration methods have been applied: the first method uses a commercial AFM calibration grid for a rapid but relatively low accuracy calibration and the second method uses the lattice of muscovite mica (0.5 nm) for a finer precision calibration. All the experiments and results presented in this paper were obtained with a Cypher ES AFM (Asylum Research, Oxford Instruments, Santa Barbara, USA) equipped with photothermal tip excitation. The choice of Cypher as a test AFM is motivated by the relatively small sample space available, which illustrates the versatility of the HF-stage.

1. Calibration method 1

Imaging of the pitch's edge of a calibration grid is done using the AFM standard imaging mode. By placing the grid so that the pitch appears vertical in the image, the edge makes a straight line that acts as a reference. The HF-stage is then used to add a perpendicular sinusoidal oscillation with low frequencies (1–10 Hz) and different voltage amplitudes to allow direct visualization of the associated displacement (Fig. 9). When the stage unidirectional motion is switched ON, the grid's edge appears as a sawtooth pattern whose
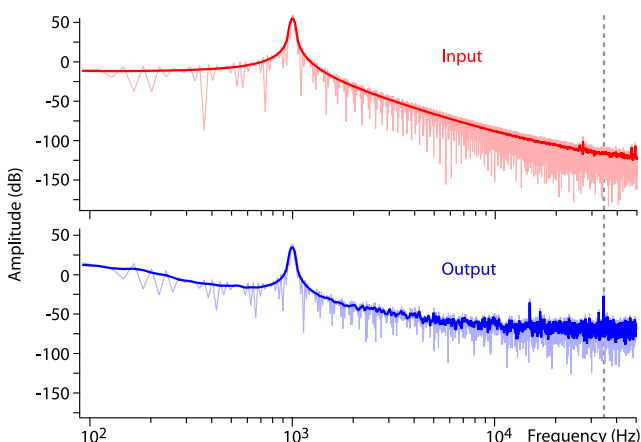
FIG. 7. Stage operation at the 1 kHz, 1 V input (top). The measured frequency response of the stage tracks the signal accurately with a faint peak around the stage's resonance frequency (dashed vertical line). The solid lines represent a two-pass binomial smoothing of the raw data (lighter background).
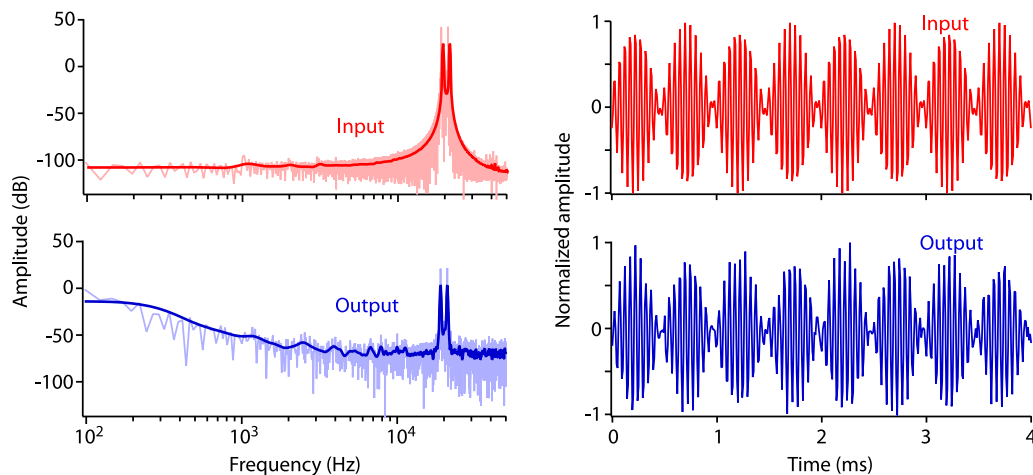
FIG. 8. Frequency response of the stage to the 20 kHz sinusoidal signal modulated by a sinusoidal 1 kHz, 1 V input. The response is shown in the frequency (left) and temporal (right) domains, with in both cases the signal imposed on the stack piezo (top) and the stage response (bottom). In the frequency domain, the solid lines represent a two-pass binomial smoothing of the raw data (lighter background).

amplitude is that of the HF-stage motion. The process has to be carried out separately for both the X and Y axes of the stage, rotating the calibration grid by $90°$ in between.

2. Calibration method 2

For the finer calibration of the HF-stage displacement, the stage can be used as an AFM scanner over a mica sample. This is achieved by operating the AFM normally for imaging but with an image scan size set to 0 and only the HF-stage operating. Having the stage and acquisition frequencies synchronized, the actual captured image is the result of the nanopositioner line scan along the axis of interest. The image is then formed by a succession of profiles taken over the mica lattice. Here, the data are acquired in a 10 mM KCl solution (Fig. 10) with the horizontal x axis taken as a reference for the calibration, while the y axis is not real spatial data. A distortion is visible

in Fig. 10 due to an imperfect synchronization between the AFM acquisition software and the oscillation of the stage, both working independently.

### D. Operation in conjunction with the AFM: Possibilities, limitations, and resolution

In order for the HF-stage to function effectively for lateral dynamic sensing, its oscillations should have a minimal impact on the AFM spatial resolution. In typical AFM applications, dynamical sensing with a vibrating cantilever is carried out using small amplitude (<1 nm) oscillations. Here, if applying directional lateral oscillations of comparable amplitude, we expect the imaging resolution of the AFM to be minimally affected.

To test this hypothesis, we acquired AFM high resolution images in amplitude modulation and switched ON the HF-stage
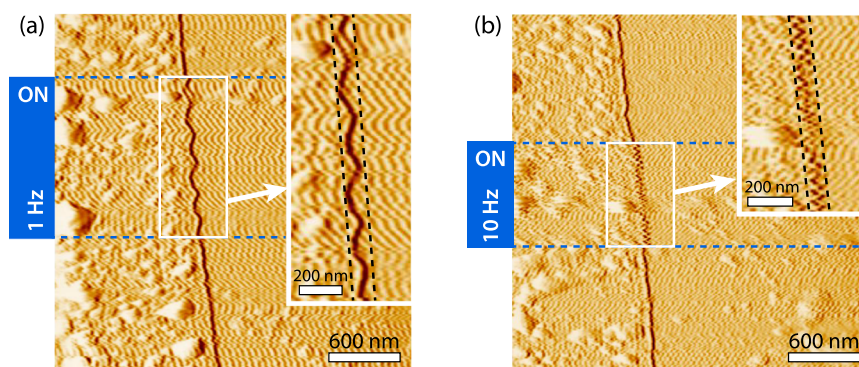
FIG. 9. Example of calibration using a standard calibration grid. While the AFM scans the step-edge of the grid, the HF-stage is switched ON, operating with a unidirectional sinusoidal motion in the direction perpendicular to the step edge (horizontal here). At low frequencies, this results in the edge appearing as a sawtooth pattern whose amplitude is that of the stage oscillation motion (distance between dashed black lines in the inset). The process is illustrated here at 1 (a) and 10 Hz (b). The regions highlighted in light blue indicate the part of the image where the stage is ON. From this figure, a calibration of 5.13 nm/V is derived for the HF-stage. Both images are amplitude images for better contrast on the step-edge. No image processing has been applied.
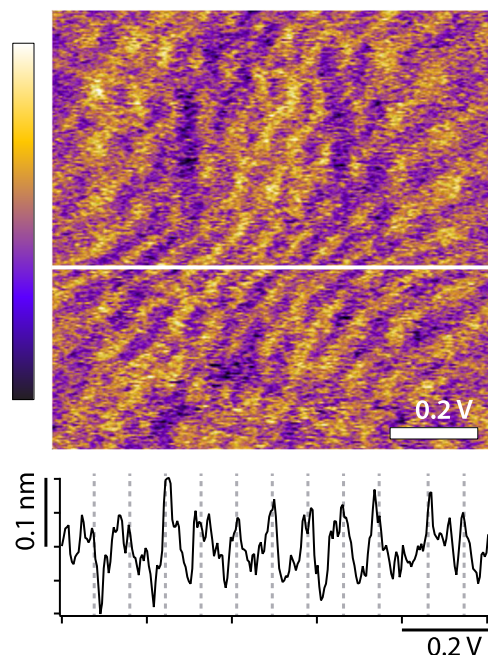
FIG. 10. Representative topographic image used for the stage calibration using the mica lattice as a reference. The HF-stage oscillation provides the movement along the x axis, with the data acquired using the AFM software. Imperfect synchronization between the stage oscillations and the acquisition software causes distortions between the lines, and calibration profiles are selected in the less distorted regions (white profile line). From the mica periodicity, a fine calibration of 5.67 nm/V is found for small (<10 nm) amplitudes. Here, the HF-stage oscillation is driven at 1 V peak to peak with a frequency of 6 Hz. The color scale represents a total height variation of 0.2 nm. No image processing has been applied apart for tilt correction (line flattening).

only for the central region of the AFM image so as to allow for a direct comparison of the stage's impact on the imaging resolution. When switched ON, the stage works in "vortex" mode,[59] with a fast oscillation (frequency ν_{sweep}) modulated by a slower oscillation (frequency ν_{vortex}) applied to both the X and Y stage directions with a defined phase difference. In vortex mode, the faster frequency carries out the dynamical lateral sensing and its magnitude is comparable to the cantilever vertical vibration frequency. The slower modulation (ν_{vortex}) is used to systematically probe all the lateral directions at a given location by progressively changing the angle of the lateral sweep until it has completed a full revolution (the vortex) over a period of $1/\nu_{vortex}$.[59] To test the suitability of the HF-stage for vortex scanning, ν_{sweep} was varied systematically across frequencies, below, at, and above the resonance of the AFM cantilever. Figure 11 shows high resolution images in liquid acquired on mica [Figs. 11(a) and 11(b)] and purple membranes [Fig. 11(d)] with ν_{vortex} = 750–1000 Hz and ν_{sweep} varying between 6 and 40.5 kHz with an amplitude of ~0.5 nm peak to peak. Mica is ideal to test atomic-level resolution on hard samples,[22,80,81] whereas the bacteriorhodopsin trimers of purple membranes offer the equivalent for soft interfaces.[81–85] On both samples, high resolution is maintained for ν_{sweep} below and above the cantilever's resonance, with the apparition of noise when ν_{sweep} is exactly at the resonance. This is to

be expected due to some coupling between the lateral and vertical oscillations through the liquid. When ν_{sweep} matches the cantilever's resonance, the vertical oscillation is stimulated, but the coupling depends on the geometry of the system, making it difficult to derive any reliable lateral information. Due to the relatively low resonance of most cantilevers in liquid, this can be limiting for using higher ν_{sweep} frequencies with the risk of stimulating higher eigenmodes of the cantilever. We therefore tested the same vortex operation but with the cantilever vibrating at its second eigenmode [Fig. 11(c)]. Better resolution is achieved with the second eigenmode, potentially widening the operational possibilities of the system. Noise issues become less important even when ν_{sweep} matches the frequency of the first eigenmode and for higher oscillation amplitudes [Fig. 11(c)]. However, noise flares up again when ν_{sweep} matches the frequency of the second eigenmode driving the cantilever.

E. Example of successful measurements

To demonstrate the capabilities of the HF-stage in augmenting standard AFM measurements, we used it in vortex mode to map the preferred flow directions adopted by different aqueous solutions at the surface of graphite [Highly Ordered Pyrolytic Graphite (HOPG)] and graphene oxide (GO) at the nanoscale. A detailed discussion of this analysis and its implications together with further results is given elsewhere.[59]

In short, the idea is to exploit the fact that when the AFM tip moves across or through the interfacial liquid and pushes the liquid molecules, the resistance it experiences is related to the molecules' ability to move along the solid's surface.[86] In aqueous solutions, there is a direct relationship between the energy needed to displace the liquid molecules located immediately under the tip and the local affinity of the liquid for the solid.[87]

Practically, this is achieved here by operating the AFM in amplitude modulation while using the HF-stage in a vortex mode of operation to explore the resistance of the fluid along each direction for each pixel of the AFM image. The relative resistance of the fluid in a given direction is obtained from the energy dissipation associated with the tip vertical oscillation, while the stage oscillates laterally along the direction of interest.[86] Here, because we operate the AFM in amplitude modulation, changes in energy dissipation can be measured from changes in the tip oscillation's phase,[19,22,88,89] but the approach can be achieved in any mode where the local dissipation can be measured.[90]

The method is used here to investigate the flow of aqueous solutions containing KCl and MgCl$_2$ at the interface with GO flakes. K$^+$ and Mg^{2+} are well-known to behave differently when sieved through membranes composed of stacked GO sheets,[91,92] a behavior explained by differences in the ions' hydration structures when moving along the interface with GO.[93–95] The results (Fig. 12) show measurements conducted consecutively in solutions containing KCl and MgCl$_2$ with the same tip on the same GO flake adsorbed onto an HOPG substrate. In each solution, four results are presented: the topographic image [Fig. 12(a) for KCl and (g) for MgCl$_2$], the associated phase image standard to the amplitude modulation AFM [(b) for KCl and (h) for MgCl$_2$], a quantitative directionality image indicating the relative importance of a possible directional flow at every location of the surface [(d) for KCl and (j) for MgCl$_2$], and the preferred angle associated with this flow [(e) for KCl and (k)
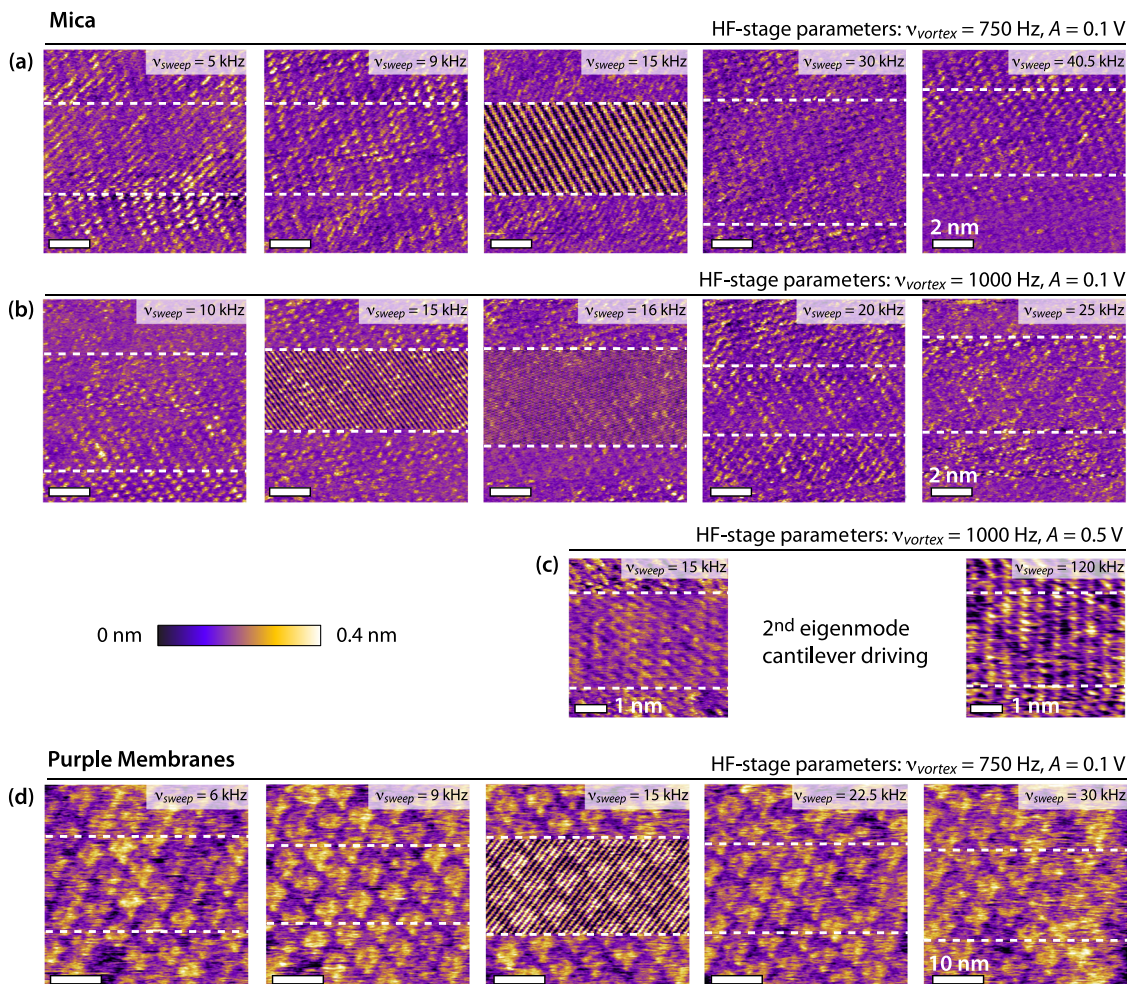
FIG. 11. Evaluation of the impact of the HF-stage on the AFM high resolution capabilities in liquid when used in vortex mode. A commercial RC 800PSA (Olympus, Japan) with eigenfrequencies in water of 15.6 (first) and 120 kHz (second) is used for all the images, operated in amplitude modulation. The stage is switched ON in vortex mode in the central part of the image only (between dashed lines) to offer some comparison. When the cantilever is driven on mica at its first eigenfrequency [(a) and (b)], high resolution is possible with a stage oscillation amplitude of 0.1 Vpp (~0.5 nm) except at the frequency of the eigenmode driven. When operating the cantilever at its second eigenmode (c), high resolution can be preserved with a larger applied voltage (0.5 Vpp), but it deteriorates again when reaching the driving frequency of the cantilever. The same result can be obtained on soft purple membranes of halobacterium salinarum (d), here with the cantilever operated at its first eigenmode.

for MgCl$_2$]. The vortex scanning is switched ON only in the lower part of each image to allow for comparison. In the topography, the GO flake appears slightly higher than the HOPG background. This is confirmed by the phase contrast between both materials with the GO appearing darker [Figs. 12(b) and 12(h)]. This is expected since the phase is linked to the interfacial energy dissipation and hence sensitive to the local flow dynamics. In KCl, this is also visible in the directionality [Fig. 12(d), top] with marginally higher values observed on HOPG compared to GO, reflecting a higher lateral flow of the solution over the HOPG, albeit in random directions due to local fluctuations. To better quantify the differences in preferential flow angles between GO and HOPG, the phase information was used to create a mask that objectively distinguishes GO and HOPG and angle probability distributions were calculated in both regions

[(c) for KCl and (i) for MgCl$_2$]. The measurements on HOPG are expected to be direction independent due to the large slip length of the aqueous solution[86] and can hence serve as a reference to discount experimental bias coming from geometrical factors (tip shape, sample tilt, and imperfect oscillation axis) and chemical inhomogeneities on the tip.[96] In KCl, no clear difference can be seen between the angle distributions obtained on HOPG and GO [Fig. 12(c)], indicating the absence of a quantifiable preferential flow direction in KCl when taking the ratio of the two distributions [Fig. 12(f)]. Both distributions still indicate a preferred angle of ~20°, revealing the extent of the experimental bias.

In MgCl$_2$, the same measurement shows a slight increase in directionality over the GO flake [Fig. 12(d)]. This in itself indicates a difference in the interfacial behavior of the solution compared to
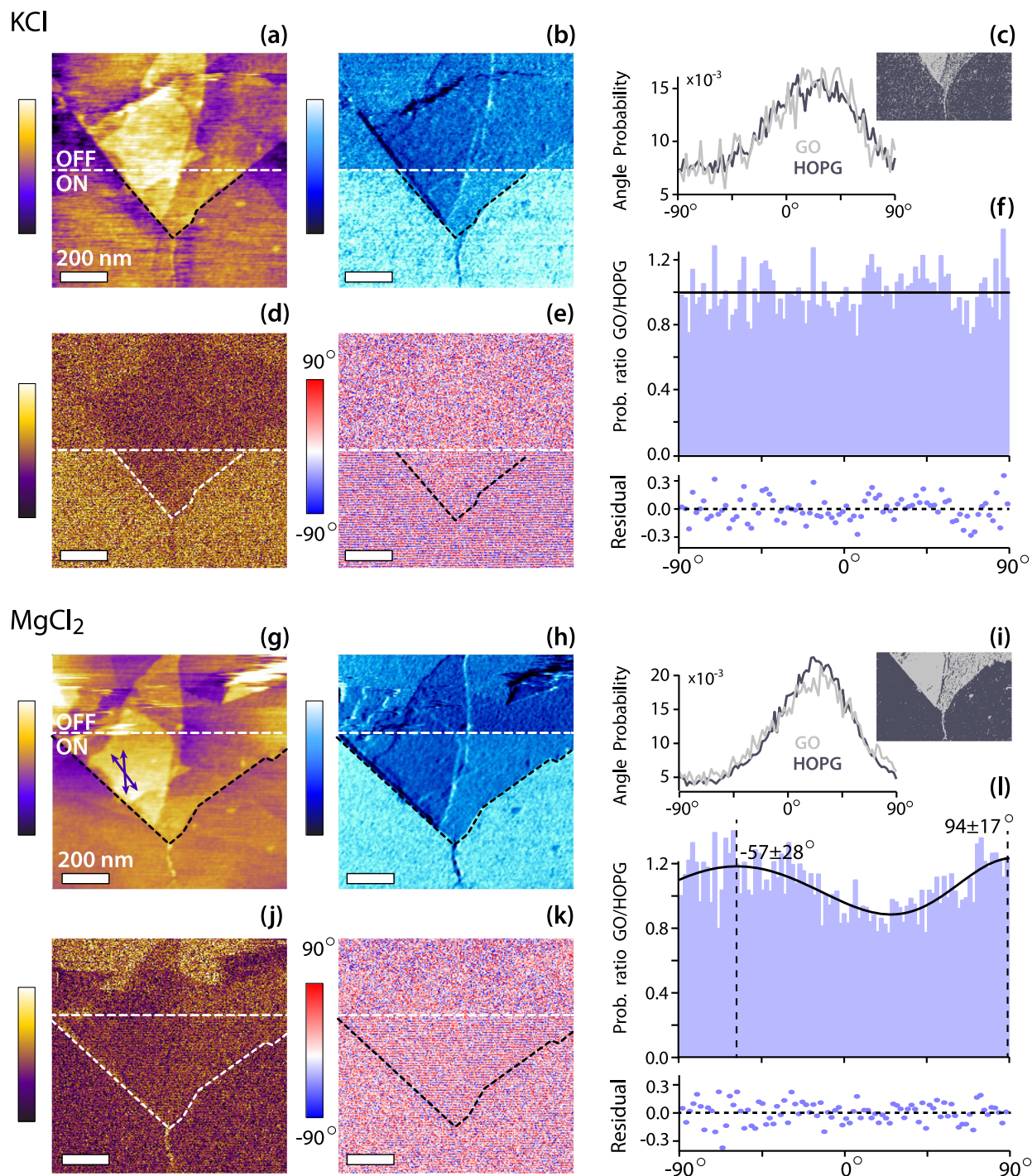
FIG. 12. Measurement of the preferential flow direction on GO/HOPG. The data were acquired over the same location with the same cantilever/tip (Scanasyst FLUID+, Bruker AFM Probes, Camarillo, USA) and in operating conditions as close as possible in the two solutions. The measurements were first conducted in 10 mM KCl, followed by extensive rinsing with 10 mM MgCl$_2$ and subsequent measurements in the 10 mM MgCl$_2$ solution. In both solutions, the topography [(a) and (g)], the associated phase [(b) and (h)], the existence of directionality [(d) and (j)], and its associated preferred flow angle [(e) and (k)] are shown, with the HF-stage ON only in the lower part of the image (white dashed line). The GO flake is highlighted with a black dashed line. The vortex operation reduces the directionality on GO compared with HOPG in KCl, as expected for a hydrophilic substrate with no preferential flow direction. This is reversed in MgCl$_2$, indicating the existence of a preferred directionality over GO, as confirmed by the angle distribution [(c) and (i)] and the associated distribution probability [(f) and (l)]. The color scale bars are identical for both solutions and represent height variations of 4 nm (topography), 10° (phase), and 0.1 < D < 0.45 (directionality). v_{sweep} = 40 kHz with a sweeping amplitude of ~1.5 nm peak to peak.

KCl. The preferential angle analysis [Fig. 12(i)] shows subtle differences between the two angle distributions whose ratio reveals two distinct maxima at ~120° from each other [Fig. 12(l)] and aligned with the edges of the GO flake [purple arrows in (g)]. This suggests a correlation between the preferential flow directions and the lattice orientation of the GO.

Overall, these results indicate that in the presence of Mg^{2+} ions, the interfacial flow parallel to GO flakes enhances when along directions that are in registry with the GO lattice. This is, however, not the case for K^+ ions. The molecular origins and implications of this ion-specific directionality are discussed elsewhere,[59] but the present results illustrate the capabilities of the HF-stage to derive information otherwise inaccessible with a standard AFM.

III. DISCUSSION

The high-frequency piezo-based flexural stage developed in this study acts as an add-on to existing AFMs, augmenting the capabilities of dynamic modes by enabling the tip to vibrate in any desired direction. This is done by adding a small directional in-plane oscillation to the vertically vibrating AFM tip operated by a standard AFM. Using suitable materials and design, the HF-stage is designed small enough to fit directly atop the scanner of most commercial AFMs.

The operating frequency range of a scanner is typically taken below its natural resonance, here yielding a bandwidth of ~35 kHz. However, when operated as intended for the present work, the stage uses small displacements of typically less than 2 nm peak to peak. As a result, meaningful data can be derived even above resonance (usually within a <15% range) without significant distortion problems (e.g., 40 kHz in Fig. 12). Successful trials at 120 kHz [Fig. 9(c)] suggest that even higher frequencies can be used in these conditions, but this remains to be confirmed with quantitative results, such as those presented in Fig. 12. It is also worth noting that the natural resonance frequency of the stage can be increased by adjusting with parameters such as the mass of the stage, the mass of the piezo elements, and their respective stiffness [Eq. (1) and Refs. 1, 2, 78, and 79].

When implementing the HF-stage operation with that of the AFM, the main challenge to derive meaningful results comes from the synchronization of both systems, including for data acquisition. The fact that the stage allows acquiring directional information as the AFM tip is located at the same location requires the AFM data collected at that location to be split in suitable time intervals, each associated with a given lateral direction. This is not given as standard with commercial AFM software and may require AFM-specific developments. With this paper, we therefore provide our basic Labview code used to drive the HF-stage and analyze the data in vortex mode. This software operated in conjunction with an AFM from Oxford Instruments but could be easily adapted.

The HF-stage was used successfully here to derive directional information about the nanoscale flow patterns adopted by ionic aqueous solutions at the surface of HOPG and GO, reproducibly identifying a preferred motion in registry with the GO lattice in the presence of Mg^{2+} ions.[59] In order to derive meaningful flow information, most of the tip apex (>20 nm^2) is likely to contribute to the measurement, but atomic-level resolution is still possible thanks to

localized asperities[22,82] or stable hydration sites[96] located at the tip apex. High-resolution could be demonstrated on hard mica and soft purple membrane samples in solution with the HF-stage operating. A loss of resolution is only visible if the amplitude of the oscillation imposed by the stage becomes larger than the distance between the features to be resolved or if the stage is operated at the same frequency as the vertical oscillation of the tip. The last issue may be related to the lack of phase synchronization between both motions, thereby introducing significant anharmonicities to the overall tip composed oscillation.

Beyond the proofs of principles established in the present work, there is still significant scope for improvement and exploration of the method's possibilities. First, the HF-stage itself can be improved for higher resonance and lower noise operation. A major improvement would also see phase synchronization between the vertical and lateral oscillations to enable for more accurate measurements, including a full quantification of the orientation and direction (forward or backward) being probed along that particular orientation. Here, to allow for reliable measurements, a full vortex revolution is carried out at each pixel, making the process relatively slow, typically 1 line/s in imaging. The fundamental limit for faster measurements comes from the AFM electronics and the response (damping) timescale of the oscillating tip in liquid. Being still far from these limitations here, the timescale of the measurements can still be improved by an order of magnitude using short commercial cantilevers with high-end AFMs.

Second, the HF-stage can be exploited to modulate and enhance the spatial resolution and explore the dynamics of different solvation layers at interfaces in solution. This is because the interfacial liquid itself plays an important role in AFM resolution at solid–liquid interfaces.[15,22,80,97] On soft samples, such as biomembranes, this can be further exploited to preserve the sample by playing with the viscoelastic properties of the interfacial water that then acts as a lubrication, energy absorbing layer.[98]

Finally, the interplay between the sweep and tip oscillation frequencies needs to be investigated in depth, especially its impact on the measurement process and on the result. Here, the measurements were conducted in amplitude modulation for the demonstrated high-resolution capabilities and the robustness of the mode, but the method is not specific to any imaging mode either ON or OFF resonance, leaving a large ground to be explored in future studies.

IV. CONCLUSION

The present study has described the development of the miniature flexure-based two-dimensional HF-stage for high resolution directional dynamic sensing with an AFM, also in a liquid environment. The HF-stage is designed, built, and tested with the aim of augmenting the measurement capabilities of the standard dynamic mode AFM by adding a controlled lateral component to the otherwise vertical tip oscillation. To illustrate the potential of the stage for in-plane dynamical sensing with high spatial resolution, we use it here to quantify the nanoscale flow patterns preferentially adopted by aqueous solutions along the surface of immersed graphene oxide. The method is compatible with most existing AFMs and does not preclude high-resolution imaging.

DATA AVAILABILITY

The data that support the findings of this study and the software used to drive the stage (Labview) are available from the corresponding author upon reasonable request.

REFERENCES

[1] S. Devasia, E. Eleftheriou, and S. O. R. Moheimani, "A survey of control issues in nanopositioning," IEEE Trans. Control Syst. Technol. **15**, 802–823 (2007).

[2] C. Shi, D. K. Luu, Q. Yang, J. Liu, J. Chen, C. Ru, S. Xie, J. Luo, J. Ge, and Y. Sun, "Recent advances in nanorobotic manipulation inside scanning electron microscopes," Microsyst. Nanoeng. **2**, 16024 (2016).

[3] W. Zhang, M. Pang, and C. Ru, "Nanopositioning for lithography and data storage," in *Nanopositioning Technologies: Fundamentals and Applications*, edited by C. Ru, X. Liu, and Y. Sun (Springer International, 2016), pp. 381–409.

[4] G. Binnig, H. Rohrer, C. Gerber, and E. Weibel, "Tunneling through a controllable vacuum gap," Appl. Phys. Lett. **40**, 178–180 (1982).

[5] G. Binnig, H. Rohrer, C. Gerber, and E. Weibel, "Surface studies by scanning tunneling microscopy," Phys. Rev. Lett. **49**, 57 (1982).

[6] G. Binnig, C. F. Quate, and C. Gerber, "Atomic force microscope," Phys. Rev. Lett. **56**, 930 (1986).

[7] C. Gerber and H. P. Lang, "How the doors to the nanoworld were opened," Nat. Nanotechnol. **1**, 3–5 (2006).

[8] J. K. H. Hörber and M. Miles, "Scanning probe evolution in biology," Science **302**, 1002–1005 (2003).

[9] F. Besenbacher, J. V. Lauritsen, T. R. Linderoth, E. Lægsgaard, R. T. Vang, and S. Wendt, "Atomic-scale surface science phenomena studied by scanning tunneling microscopy," Surf. Sci. **603**, 1315–1327 (2009).

[10] G. Binnig and D. P. E. Smith, "Single-tube three-dimensional scanner for scanning tunneling microscopy," Rev. Sci. Instrum. **57**, 1688–1689 (1986).

[11] S. O. R. Moheimani, "Invited review article: Accurate and fast nanopositioning with piezoelectric tube scanners: Emerging trends and future challenges," Rev. Sci. Instrum. **79**, 071101 (2008).

[12] M. Mohammadzaheri and A. AlQallaf, "Nanopositioning systems with piezoelectric actuators, current state and future perspective," Sci. Adv. Mater. **9**, 1071–1080 (2017).

[13] E. Vinge, *Nanopositioning: Construction and Analysis of a Piezoelectric Tube Actuator* (Norwegian University of Science and Technology, 2009).

[14] C. A. Amo, A. P. Perrino, A. F. Payam, and R. Garcia, "Mapping elastic properties of heterogeneous materials in liquid with angstrom-scale resolution," ACS Nano **11**, 8650–8659 (2017).

[15] W. Trewby, J. Faraudo, and K. Voïtchovsky, "Long-lived ionic nanodomains can modulate the stiffness of soft interfaces," Nanoscale **11**, 4376–4384 (2019).

[16] W. Foster, K. Miyazawa, T. Fukuma, H. Kusumaatmaja, and K. Voïtchovsky, "Self-assembly of small molecules at hydrophobic interfaces using group effect," Nanoscale **12**, 5452–5463 (2020).

[17] T. Fukuma, Y. Ueda, S. Yoshioka, and H. Asakawa, "Atomic-scale distribution of water molecules at the mica-water interface visualized by three-dimensional scanning force microscopy," Phys. Rev. Lett. **104**, 016101 (2010).

[18] F. J. Giessibl, "Advances in atomic force microscopy," Rev. Mod. Phys. **75**, 949 (2003).

[19] R. García and R. Pérez, "Dynamic atomic force microscopy methods," Surf. Sci. Rep. **47**, 197–301 (2002).

[20] W. Liang, H. Shi, X. Yang, J. Wang, W. Yang, H. Zhang, and L. Liu, "Recent advances in AFM-based biological characterization and applications at multiple levels," Soft Matter **16**, 8962–8984 (2020).

[21] R. García, R. Magerle, and R. Perez, "Nanoscale compositional mapping with gentle forces," Nat. Mater. **6**, 405–411 (2007).

[22] K. Voïtchovsky, J. J. Kuna, S. A. Contera, E. Tosatti, and F. Stellacci, "Direct mapping of the solid-liquid adhesion energy with subnanometre resolution," Nat. Nanotechnol. **5**, 401–405 (2010).

[23] M. Ricci, P. Spijker, and K. Voïtchovsky, "Water-induced correlation between single ions imaged at the solid–liquid interface," Nat. Commun. **5**, 4400 (2014).

[24] M. Ricci, W. Trewby, C. Cafolla, and K. Voïtchovsky, "Direct observation of the dynamics of single metal ions at the interface with solids in aqueous solutions," Sci. Rep. **7**, 43234 (2017).

[25] M. Ricci, R. A. Quinlan, and K. Voïtchovsky, "Sub-nanometre mapping of the aquaporin–water interface using multifrequency atomic force microscopy," Soft Matter **13**, 187–195 (2017).

[26] K. Voïtchovsky, "Anharmonicity, solvation forces, and resolution in atomic force microscopy at the solid-liquid interface," Phys. Rev. E **88**, 022407 (2013).

[27] K. Voïtchovsky, D. Giofrè, J. José Segura, F. Stellacci, and M. Ceriotti, "Thermally-nucleated self-assembly of water and alcohol into stable structures at hydrophobic interfaces," Nat. Commun. **7**, 13064 (2016).

[28] S.-H. Loh and S. P. Jarvis, "Visualization of ion distribution at the mica–electrolyte interface," Langmuir **26**, 9176–9178 (2010).

[29] J. Schütte, P. Rahe, L. Tröger, S. Rode, R. Bechstein, M. Reichling, and A. Kühnle, "Clear signature of the (2 × 1) reconstruction of calcite (10$\overline{1}$4)," Langmuir **26**, 8295–8300 (2011).

[30] H. Yamada, K. Kobayashi, T. Fukuma, Y. Hirata, T. Kajita, and K. Matsushige, "Molecular resolution imaging of protein molecules in liquid using frequency modulation atomic force microscopy," Appl. Phys. Express **2**, 095007 (2009).

[31] Y. Song and B. Bhushan, "Dynamic analysis of torsional resonance mode of atomic force microscopy and its application to in-plane surface property extraction," Microsyst. Technol. **12**, 219–230 (2006).

[32] L. Collins, M. Ahmadi, T. Wu, B. Hu, S. V. Kalinin, and S. Jesse, "Breaking the time barrier in kelvin probe force microscopy: Fast free force reconstruction using the G-mode platform," ACS Nano **11**, 8717–8729 (2017).

[33] K. Honbo, S. Ogata, T. Kitagawa, T. Okamoto, N. Kobayashi, I. Sugimoto, S. Shima, A. Fukunaga, C. Takatoh, and T. Fukuma, "Visualizing nanoscale distribution of corrosion cells by open-loop electric potential microscopy," ACS Nano **10**, 2575–2583 (2016).

[34] G. B. Kaggwa, P. C. Nalam, J. I. Kilpatrick, N. D. Spencer, and S. P. Jarvis, "Impact of hydrophilic/hydrophobic surface chemistry on hydration forces in the absence of confinement," Langmuir **28**, 6589–6594 (2012).

[35] S. H. Khan, E. L. Kramkowski, and P. M. Hoffmann, "NaCl-dependent ordering and dynamic mechanical response in nanoconfined water," Langmuir **32**, 10802–10807 (2016).

[36] F. Liu, C. Zhao, F. Mugele, and D. van den Ende, "Amplitude modulation atomic force microscopy, is acoustic driving in liquid quantitatively reliable?," Nanotechnology **26**, 385703 (2015).

[37] C. Cafolla, W. Foster, and K. Voïtchovsky, "Lubricated friction around nanodefects," Sci. Adv. **6**, eaaz3673 (2020).

[38] C. Cafolla and K. Voïtchovsky, "Impact of water on the lubricating properties of hexadecane at the nanoscale," Nanoscale **12**, 14504–14513 (2020).

[39] R. Szoszkiewicz and E. Riedo, "Nanoscopic friction as a probe of local phase transitions," Appl. Phys. Lett. **87**, 033105–033103 (2005).

[40] L. Bocquet and J.-L. Barrat, "Flow boundary conditions from nano- to micro-scales," Soft Matter **3**, 685–693 (2007).

[41] J.-L. Barrat and L. Bocquet, "Large slip effect at a nonwetting fluid-solid interface," Phys. Rev. Lett. **82**, 4671–4674 (1999).

[42] L. Bocquet and E. Charlaix, "Nanofluidics, from bulk to interfaces," Chem. Soc. Rev. **39**, 1073 (2010).

[43] T. Osswald and N. Rudolph, *Polymer Rheology* (Hanser Publications, 2015).

[44] T. Fukuma and R. Garcia, "Atomic- and molecular-resolution mapping of solid–liquid interfaces by 3D atomic force microscopy," ACS Nano **12**, 11785–11797 (2018).

[45]T. Ando and T. Uchihashi, "High-speed atomic force microscopy," in *Handbook of Single-Molecule Biophysics*, edited by P. Hinterdorfer and A. Oijen (Springer, 2009), pp. 487–520.

[46]M. J. Rost, L. Crama, P. Schakel, E. van Tol, G. B. E. M. van Velzen-Williams, C. F. Overgauw, H. ter Horst, H. Dekker, B. Okhuijsen, M. Seynen, A. Vijftigschild, P. Han, A. J. Katan, K. Schoots, R. Schumm, W. van Loo, T. H. Oosterkamp, and J. W. M. Frenken, "Scanning probe microscopes go video rate and beyond," Rev. Sci. Instrum. **76**, 053710 (2005).

[47]P. K. Hansma, G. Schitter, G. E. Fantner, and C. Prater, "High-speed atomic force microscopy," Science **314**, 601 (2006).

[48]G. Schitter, F. Allgöwer, and A. Stemmer, "A new control strategy for high-speed atomic force microscopy," Nanotechnology **15**, 108–114 (2003).

[49]G. E. Fantner, G. Schitter, J. H. Kindt, T. Ivanov, K. Ivanova, R. Patel, N. Holten-Andersen, J. Adams, P. J. Thurner, I. W. Rangelow, and P. K. Hansma, "Components for high speed atomic force microscopy," Ultramicroscopy **106**, 881 (2006).

[50]M. B. Viani, L. I. Pietrasanta, J. B. Thompson, A. Chand, I. C. Gebeshuber, J. H. Kindt, M. Richter, H. G. Hansma, and P. K. Hansma, "Probing protein-protein interactions in real time," Nat. Struct. Mol. Biol. **7**, 644 (2000).

[51]Y. K. Yong, S. O. R. Moheimani, B. J. Kenton, and K. K. Leang, "Invited review article: High-speed flexure-guided nanopositioning: Mechanical design and control issues," Rev. Sci. Instrum. **83**, 121101 (2012).

[52]T. Uchihashi, T. Ando, and H. Yamashita, "Fast phase imaging in liquids using a rapid scan atomic force microscope," Appl. Phys. Lett. **89**, 213112 (2006).

[53]T. Uchihashi, N. Kodera, H. Itoh, H. Yamashita, and T. Ando, "Feed-forward compensation for high-speed atomic force microscopy imaging of biomolecules," Jpn. J. Appl. Phys., Part 1 **45**, 1904–1908 (2006).

[54]T. Uchihashi, N. Kodera, and T. Ando, "Guide to video recording of structure dynamics and dynamic processes of proteins by high-speed atomic force microscopy," Nat. Protoc. **7**, 1193–1206 (2012).

[55]T. Uchihashi, R. Iino, T. Ando, and H. Noji, "High-speed atomic force microscopy reveals rotary catalysis of rotorless F1-ATPase," Science **333**, 755–758 (2011).

[56]H. Yamashita, K. Voïtchovsky, T. Uchihashi, S. A. Contera, J. F. Ryan, and T. Ando, "Dynamics of bacteriorhodopsin 2D crystal observed by high-speed atomic force microscopy," J. Struct. Biol. **167**, 153–158 (2009).

[57]K. Voïtchovsky, S. A. Contera, and J. F. Ryan, "Lateral coupling and cooperative dynamics in the function of the native membrane protein bacteriorhodopsin," Soft Matter **5**, 4899–4904 (2009).

[58]A. P. Nievergelt, N. Banterle, S. H. Andany, P. Gönczy, and G. E. Fantner, "High-speed photothermal off-resonance atomic force microscopy reveals assembly routes of centriolar scaffold protein SAS-6," Nat. Nanotechnol. **13**, 696–701 (2018).

[59]L. Piantanida, A. F. Payam, J. Zhong, and K. Voitchovsky, "Nanoscale mapping of the directional flow patterns at liquid-solid interfaces," Phys. Rev. Appl. **13**, 064003 (2020).

[60]A. D. L. Humphris, M. J. Miles, and J. K. Hobbs, "A mechanical microscope: High-speed atomic force microscopy," Appl. Phys. Lett. **86**, 034106 (2005).

[61]J. D. Adams, A. Nievergelt, B. W. Erickson, C. Yang, M. Dukic, and G. E. Fantner, "High-speed imaging upgrade for a standard sample scanning atomic force microscope using small cantilevers," Rev. Sci. Instrum. **85**, 093702 (2014).

[62]G. Schitter and A. Stemmer, "Identification and open-loop tracking control of a piezoelectric tube scanner for high-speed scanning-probe microscopy," IEEE Trans. Control Syst. Technol. **12**, 449–454 (2004).

[63]B. J. Kenton and K. K. Leang, "Design and control of a three-Axis serial-kinematic high-bandwidth nanopositioner," IEEE/ASME Trans. Mechatron. **17**, 356–369 (2012).

[64]B. J. Kenton, "Design, characterization, and control of a high-bandwidth serial-kinematic nanopositioning stage for scanning probe microscopy applications," M.Sc. thesis, University of Nevada, Reno, 2010.

[65]B. J. Kenton and K. K. Leang, "Flexure design using metal matrix composite materials: Nanopositioning example," in *IEEE International Conference on Robotics and Automation* (IEEE, 2012), pp. 4768–4773.

[66]N. Kodera, H. Yamashita, and T. Ando, "Active damping of the scanner for high-speed atomic force microscopy," Rev. Sci. Instrum. **76**, 053708 (2005).

[67]A. Farokh Payam, P. Biglarbeigi, A. Morelli, P. Lemoine, J. McLaughlin, and D. Finlay, "Data acquisition and imaging using wavelet transform: A new path for high speed transient force microscopy," Nanoscale Adv. **3**, 383 (2021).

[68]D. Knebel, M. Amrein, K. Voigt, and R. Reichelt, "A fast and versatile scan unit for scanning probe microscopy," Scanning **19**, 264–268 (2006).

[69]L. M. Picco, L. Bozec, A. Ulcinas, D. J. Engledew, M. Antognozzi, M. A. Horton, and M. J. Miles, "Breaking the speed limit with atomic force microscopy," Nanotechnology **18**, 044030 (2006).

[70]Y. Wu, J. Shi, C. Su, and Q. Zou, "A control approach to cross-coupling compensation of piezotube scanners in tapping-mode atomic force microscope imaging," Rev. Sci. Instrum. **80**, 043709 (2009).

[71]T. Ando, N. Kodera, Y. Naito, T. Kinoshita, K. Furuta, and Y. Y. Toyoshima, "A high-speed atomic force microscope for studying biological macromolecules in action," Chem. Phys. Chem. **4**, 1196–1202 (2003).

[72]T. Ando, T. Uchihashi, and T. Fukuma, "High-speed atomic force microscopy for nano-visualization of dynamic biomolecular processes," Prog. Surf. Sci. **83**, 337–437 (2008).

[73]G. Schitter, "Advanced mechanical design and control methods for atomic force microscopy in real-time," in *2007 American Control Conference* (IEEE, 2007), pp. 3503–3508.

[74]I. S. Bozchalooi, K. Youcef-Toumi, D. J. Burns, and G. E. Fantner, "Compensator design for improved counterbalancing in high-speed atomic force microscopy," Rev. Sci. Instrum. **82**, 113712 (2011).

[75]J. H. Kindt, G. E. Fantner, J. A. Cutroni, and P. K. Hansma, "Rigid design of fast scanning probe microscopes using finite element analysis," Ultramicroscopy **100**, 259–265 (2004).

[76]H. Watanabe, T. Uchihashi, T. Kobashi, M. Shibata, J. Nishiyama, R. Yasuda, and T. Ando, "Wide-area scanner for high-speed atomic force microscopy," Rev. Sci. Instrum. **84**, 053702 (2013).

[77]Y. K. Yong, "Preloading piezoelectric stack actuators in high-speed nanopositioning systems," Front. Mech. Eng. **2**, 062001 (2016).

[78]S. P. Wadikhaye, Y. K. Yong, and S. O. R. Moheimani, "Nanopositioner design using tapered flexures: A parametric study," in *2013 IEEE/ASME International Conference on Advanced Intelligent Mechatronics* (IEEE, 2013), pp. 856–861.

[79]Y. K. Yong, S. S. Aphale, and S. O. R. Moheimani, "Design, identification, and control of a flexure-based XY stage for fast nanoscale positioning," IEEE Trans. Nanotechnol. **8**, 46–54 (2009).

[80]E. J. Miller, W. Trewby, A. Farokh Payam, L. Piantanida, C. Cafolla, and K. Voïtchovsky, "Sub-nanometer resolution imaging with amplitude-modulation atomic force microscopy in liquid," J. Vis. Exp. **118**, e54924 (2016).

[81]A. F. Payam, J. R. Ramos, and R. Garcia, "Molecular and nanoscale compositional contrast of soft matter in liquid: Interplay between elastic and dissipative interactions," ACS Nano **6**, 4663–4670 (2012).

[82]D. J. Müller, D. Fotiadis, S. Scheuring, S. A. Müller, and A. Engel, "Electrostatically balanced subnanometer imaging of biological specimens by atomic force microscope," Biophys. J. **76**, 1101–1111 (1999).

[83]F. Oesterhelt, D. Oesterhelt, M. Pfeiffer, A. Engel, H. E. Gaub, and D. J. Müller, "Unfolding pathways of individual bacteriorhodopsins," Science **288**, 143–146 (2000).

[84]K. Voïtchovsky, S. A. Contera, M. Kamihira, A. Watts, and J. F. Ryan, "Differential stiffness and lipid mobility in the leaflets of purple membranes," Biophys. J. **90**, 2075–2085 (2006).

[85]S. A. Contera, K. Voïtchovsky, and J. F. Ryan, "Controlled ionic condensation at the surface of a native extremophile membrane," Nanoscale **2**, 222–229 (2010).

[86]D. Ortiz-Young, H.-C. Chiu, S. Kim, K. Voïtchovsky, and E. Riedo, "The interplay between apparent viscosity and wettability in nanoconfined water," Nat. Commun. **4**, 2482 (2013).

[87]D. M. Huang, C. Sendner, D. Horinek, R. R. Netz, and L. Bocquet, "Water slippage versus contact angle: A quasiuniversal relationship," Phys. Rev. Lett. **101**, 226101 (2008).

[88]B. Anczykowski, B. Gotsmann, H. Fuchs, J. P. Cleveland, and V. B. Elings, "How to measure energy dissipation in dynamic mode atomic force microscopy," Appl. Surf. Sci. **140**, 376–382 (1999).

[89] P. M. Hoffmann, S. Jeffery, J. B. Pethica, H. O. Ozer, and A. Oral, "Energy dissipation in atomic force microscopy and atomic loss processes," Phys. Rev. Lett. **87**, 265502 (2001).

[90] H. Söngen, R. Bechstein, and A. Kühnle, "Quantitative atomic force microscopy," J. Phys.: Condens. Matter **29**, 274001–274011 (2017).

[91] J. Abraham, K. S. Vasu, C. D. Williams, K. Gopinadhan, Y. Su, C. T. Cherian, J. Dix, E. Prestat, S. J. Haigh, I. V. Grigorieva, P. Carbone, A. K. Geim, and R. R. Nair, "Tunable sieving of ions using graphene oxide membranes," Nat. Nanotechnol. **12**, 546–550 (2017).

[92] J.-h. Song, H.-W. Yu, M.-H. Ham, and I. S. Kim, "Tunable ion sieving of graphene membranes through the control of nitrogen-bonding configuration," Nano Lett. **18**, 5506–5513 (2018).

[93] R. K. Joshi, P. Carbone, F. C. Wang, V. G. Kravets, Y. Su, I. V. Grigorieva, H. A. Wu, A. K. Geim, and R. R. Nair, "Precise and ultrafast molecular sieving through graphene oxide membranes," Science **343**, 752–754 (2014).

[94] B. Mi, "Graphene oxide membranes for ionic and molecular sieving," Science **343**, 740–742 (2014).

[95] Y. Mo, X. Zhao, and Y.-x. Shen, "Cation-dependent structural instability of graphene oxide membranes and its effect on membrane separation performance," Desalination **399**, 40–46 (2016).

[96] S. M. R. Akrami, H. Nakayachi, T. Watanabe-Nakayama, H. Asakawa, and T. Fukuma, "Significant improvements in stability and reproducibility of atomic-scale atomic force microscopy in liquid," Nanotechnology **25**, 455701 (2014).

[97] K. Voïtchovsky and M. Ricci, "High-resolution imaging of solvation structures with amplitude-modulation atomic force microscopy," Proc. SPIE **8232**, 82320O (2012).

[98] C. Cafolla and K. Voïtchovsky, "Lubricating properties of single metal ions at interfaces," Nanoscale **10**, 11831–11840 (2018).